

Low angular momentum flow model II for Sgr A*

T. Okuda *

Nishi-Asahioka-Cho 3-15-1, Hakodate 042-0915, Hokkaido, Japan

Accepted

ABSTRACT

We examine 1D two-temperature accretion flows around a supermassive black hole, adopting the specific angular momentum λ , the total specific energy ϵ and the input accretion rate $\dot{M}_{\text{input}} = 4.0 \times 10^{-6} \text{ M}_{\odot} \text{ yr}^{-1}$ estimated in the recent analysis of stellar wind of nearby stars around Sgr A*. The two-temperature flow is almost adiabatic even if we take account of the heating of electrons by ions, the bremsstrahlung cooling and the synchrotron cooling, as long as the ratio β of the magnetic energy density to the thermal energy density is taken to be as $\beta \leq 1$. The different temperatures of ions and electrons are caused by the different adiabatic indices of ions and electrons which depend on their temperature states under the relativistic regime. The total luminosity increases with increasing β and results in $\sim 10^{35} - 10^{36} \text{ erg s}^{-1}$ for $\beta = 10^{-3} - 1$. Furthermore, from 2D time-dependent hydrodynamical calculations of the above flow, we find that the irregularly oscillating shocks are formed in the inner region and that the luminosity and the mass-outflow rate vary by a factor of 2–3 and 1.5–4, respectively. The time variability may be relevant to the flare activity of Sgr A*.

Key words: accretion, accretion discs – black hole physics – hydrodynamics – radiation mechanisms: thermal – shock waves – Galaxy: centre.

1 INTRODUCTION

Sgr A* in our Galactic Centre has been extensively studied in the category of accretion processes because it is a supermassive black hole candidate in our Galaxy and has unique observational features incompatible with the standard thin disc model (Shakura-Sunyaev, hereafter S-S, model; Shakura & Sunyaev 1973). One of the remarkable features of Sgr A* is that the observed luminosity is five orders of magnitude lower than that predicted by the S-S model. Moreover, the spectrum of Sgr A* differs from the multi-temperature blackbody spectrum obtained from the S-S model. Since the observational features of Sgr A* cannot be explained by the S-S model, two types of theoretical models, namely the spherical Bondi accretion model without any net angular momentum (Bondi 1952) and the advection-dominated accretion flow (ADAF) model with high angular momentum (Narayan & Yi 1994, 1995), have been proposed (see Narayan & McClintock 2008, Yuan 2011 and Yuan & Narayan 2014 for review). Both the Bondi model and the ADAF model result in highly advected flows and the radiative efficiency is so low as to be compatible with the observations. However, in contrast with the simple Bondi model, the ADAF models were shown to be generally successful and

more advanced models (Yuan, Quataert & Narayan 2003, 2004), taking into account the parametric description of the outflow and jet, explain well the observations. The important key to these models for Sgr A* is the amount of angular momentum in the accretion flow. However, at present, we have no clear evidence for the angular momentum from observations.

The low angular momentum flow model belongs to an intermediate case between the Bondi model and the ADAF model and was applied to Sgr A* (Mościbrodzka, Das & Czerny 2006; Czerny & Mościbrodzka 2008). Assuming that the Wolf-Rayet star IRS 13 E3 is the dominant source of the matter accreting on to Sgr A* and assuming the wind temperature $T_{\text{wind}} = 1.0$ or 0.5 keV , they estimated the net angular momentum λ of $1.68\text{--}2.16$ and the Bernoulli constant ϵ of $3.97 \times 10^{-6}\text{--}1.98 \times 10^{-6}$, where the mass M of Sgr A*, the speed of light c and the Schwarzschild radius $R_g = 2GM/c^2$ are used as the units of mass, velocity and distance and G is the gravitational constant. With these flow parameters for λ and ϵ , they showed analytically that there is no continuous flow solution which attains to the event horizon, and the resulting flow would be non-stationary, but that, for the case of the angular momentum $\lambda = 1.55$ lower than the best estimates for Sgr A*, there exists a standard stationary shock solution. Motivated by their suggestion

* E-mail: bbnbh669@ybb.ne.jp

and results, we examined the low angular momentum flow model for Sgr A* using 2D time-dependent hydrodynamical calculations and discussed the results on the activity of Sgr A* (Okuda & Molteni 2012). However, in the initial model used, we assumed a constant ratio of the ion temperature T_i to the electron temperature T_e throughout the region. In this paper, without using such assumption, we solve coherently relevant differential equations of the accretion flow which include the radiative processes of heating and cooling, and examine time-dependent behaviours of the 2D accretion flow in the relevance to the activity of Sgr A*.

2 STATIONARY LOW ANGULAR MOMENTUM ACCRETION FLOW

2.1 Modeling a 1D low angular momentum flow

We consider a supermassive black hole with mass $M = 4 \times 10^6 M_\odot$ and examine a 1D low angular momentum flow around Sgr A*. We use here typical flow parameters of the specific angular momentum λ , the specific total energy ϵ and the mass accretion rate $\dot{M} = 4.0 \times 10^{-6} M_\odot \text{ yr}^{-1}$ which were estimated for the accretion flow around Sgr A* (Mościbrodzka, Das & Czerny 2006).

First, we solve the Bernoulli equation of a thin, rotating, inviscid and adiabatic accretion flow with a single temperature T and a constant angular momentum λ , find the outer and inner sonic points, and get the Mach number versus radius relation, the sound speed v_s , the thickness h of the accretion flow, the radial velocity v and the temperature T at a given radius r as is done in Chakrabarti (1989). We assume here that the accretion flow is in hydrostatic equilibrium in vertical direction

$$\frac{p}{h} = \rho \frac{GMh}{(r - R_g)^2 r}, \quad (1)$$

where p and ρ are the total gas pressure and the density. The Bernoulli constant ϵ is given by

$$\epsilon = \frac{1}{2} v^2 + \frac{1}{\gamma - 1} v_s^2 - \frac{GM}{r - R_g} + \frac{1}{2} \frac{\lambda^2}{r^2}, \quad (2)$$

where v_s and γ are the sound velocity and the specific heat ratio. In this paper, we consider two models of $\lambda = 1.68$ and $\epsilon = 3.97 \times 10^{-6}$ (model A) and $\lambda = 1.35$ and $\epsilon = 1.98 \times 10^{-6}$ (model B) in the usual nondimensional units. The Mach number versus radius relation in the models is given in figs 1 and 2 in the previous paper (Okuda & Molteni 2012). In model A, the particle which passes through the outer sonic point falls down supersonically inwards but never attains the event horizon since it makes a closed loop of the Mach number curve. On the other hand, in model B, the particle falls supersonically, jumps to a subsonic state at the shock position of $R_s \sim 20R_g$ and tends supersonically towards the event horizon.

Secondly, we adopt a two-temperature model of the accretion flow with the ion temperature T_i and the electron temperature T_e , taking account of the radiative processes of heating of electrons by ions, bremsstrahlung cooling and synchrotron cooling in the optically thin limit. From the 1D stationary equations of the inviscid and non-adiabatic accretion flow with the constant angular momentum, we have

the following differential equations of T_e , T_i and $\eta = v^2/(\frac{p}{\rho})$ (Nakamura et al. 1996):

$$\frac{d \ln T_e}{dr} = (\gamma_e - 1) \frac{A(\eta - 1) + (\gamma_i - 1)\Gamma_i(\frac{1}{2}\eta - 1)(A - B) - C}{\eta - 1 + (\frac{1}{2}\eta - 1)(\gamma_e \Gamma_e + \gamma_i \Gamma_i - 1)}, \quad (3)$$

$$\frac{d \ln T_i}{dr} = (\gamma_i - 1) \frac{B(\eta - 1) - (\gamma_e - 1)\Gamma_e(\frac{1}{2}\eta - 1)(A - B) - C}{\eta - 1 + (\frac{1}{2}\eta - 1)(\gamma_e \Gamma_e + \gamma_i \Gamma_i - 1)}, \quad (4)$$

$$\frac{d \ln \eta}{dr} = 2 \left[A - \left(\frac{1}{\gamma_e - 1} + \Gamma_e \right) \frac{d \ln T_e}{dr} - \Gamma_i \frac{d \ln T_i}{dr} \right], \quad (5)$$

$$A = \frac{4\pi \left(\frac{GM}{r} R_g T_e \Gamma_e \right)^{-1/2} (r - R_g) r}{\dot{M}} (q^{\text{ie}} - q_{\text{br}} - q_{\text{syn}}) - \frac{3}{2r} - \frac{1}{r - R_g}, \quad (6)$$

$$B = \frac{4\pi \left(\frac{GM}{r} R_g T_i \Gamma_i \right)^{-1/2} (r - R_g) r}{\dot{M}} q^{\text{ie}} - \frac{3}{2r} - \frac{1}{r - R_g}, \quad (7)$$

$$C = -\frac{(\Omega_K^2 - \Omega^2)r}{R_g(T_e + T_i)} + \frac{3}{2r} + \frac{1}{r - R_g}, \quad (8)$$

where $p = p_i + p_e$, p_i and p_e are the ion and the electron gas pressure, R_g is the gas constant, Ω is the angular velocity, Ω_K is the Keplerian angular velocity, $\dot{M} (= 4\pi r h \rho v)$ is the mass accretion rate, $\Gamma_e = T_e/(T_e + T_i)$ and $\Gamma_i = T_i/(T_e + T_i)$. γ_i and γ_e are the adiabatic indices of ions and electrons, respectively, which may differ a little depending on their temperature states and the different indices cause different temperatures of electrons and ions even in the adiabatic state as is found from equations (3) and (4) (Yuan & Narayan 2014). Here, we use that γ_e is 1.6 at $kT_e \leq m_e c^2$, that is, $T_e \leq 5.9 \times 10^9 \text{ K} (= T_c)$ where electrons are non-relativistic but is 4/3 at $kT_e \geq m_e c^2$ where electrons become relativistic, while γ_i is taken to be 1.6 throughout the region because ions remain in a non-relativistic state of $kT_i \leq m_p c^2$ (Fukue 1986). T_c is the critical electron temperature at which electrons in the non-relativistic state change into the relativistic state. q^{ei} and q_{br} are the energy transfer rate from ions to electrons by Coulomb collisions and the cooling rate of electrons by electron-ion and electron-electron bremsstrahlungs and are given as follows (Stepney & Guilbert 1983).

$$q^{\text{ie}} = 5.61 \times 10^{-32} \frac{n_e n_i (T_i - T_e)}{K_2(1/\theta_e) K_2(1/\theta_i)} \times \left[\frac{2(\theta_e + \theta_i)^2 + 1}{(\theta_e + \theta_i)} K_1\left(\frac{\theta_e + \theta_i}{\theta_e \theta_i}\right) + 2K_0\left(\frac{\theta_e + \theta_i}{\theta_e \theta_i}\right) \right] \text{ erg cm}^{-3} \text{ s}^{-1}, \quad (9)$$

$$q_{\text{br}} = q_{\text{ei}} + q_{\text{ee}}, \quad (10)$$

$$q_{\text{ei}} = 1.48 \times 10^{-22} n_e^2 F_{\text{ei}}(\theta_e) \text{ erg cm}^{-3} \text{ s}^{-1}, \quad (11)$$

$$F_{\text{ei}}(\theta_e) = \begin{cases} 1.02\theta_e^{1/2}(1 + 1.78\theta_e^{1.34}) & \text{for } \theta_e < 1, \\ 1.43\theta_e[\ln(1.12\theta_e + 0.48) + 1.5] & \text{for } \theta_e > 1, \end{cases} \quad (12)$$

$$q_{\text{ee}} = \begin{cases} 2.56 \times 10^{-22} n_e^2 \theta_e^{1.5} (1 + 1.10\theta_e + \theta_e^2 - 1.25\theta_e^{2.5}) & \text{erg cm}^{-3} \text{ s}^{-1} \text{ for } \theta_e < 1, \\ 3.40 \times 10^{-22} n_e^2 \theta_e [\ln(1.123\theta_e) + 1.28] & \text{erg cm}^{-3} \text{ s}^{-1} \text{ for } \theta_e > 1, \end{cases} \quad (13)$$

where n_e and n_i are the number density of electrons and

Table 1. Model parameters of the specific angular momentum λ , the specific total energy ϵ and the adiabatic index γ_i of ions for the accreting matter on to Sgr A*, where the radial velocity v_{out} , the Mach number M_a , the ion temperature T_i , the difference $T_i - T_e$ between the ion temperature T_i and the electron temperature T_e , the ratio β of the magnetic energy density to the thermal energy density at $R_{\text{out}} = 10^3 R_g$ in the two-temperature model are also shown.

Model	λ	ϵ	γ_i	\dot{M} ($M_\odot \text{ yr}^{-1}$)	v_{out}/c	M_a	T_i (K)	$(T_i - T_e)$ (K)	β
A	1.68	3.97×10^{-6}	1.6	4.0×10^{-6}	1.971×10^{-2}	1.3729	2.824×10^8	870	$10^{-3} - 1$
B	1.35	1.98×10^{-6}	1.6	4.0×10^{-6}	1.989×10^{-2}	1.5197	2.606×10^8	770	$10^{-3} - 1$

ions, K_0 , K_1 and K_2 are modified Bessel functions, and the dimensionless electron and ion temperature are defined by

$$\theta_e = \frac{kT_e}{m_e c^2}, \quad \theta_i = \frac{kT_i}{m_p c^2}. \quad (14)$$

q_{syn} is the synchrotron cooling rate which is given by (Narayan & Yi 1994; Esin et al. 1996)

$$\begin{aligned} q_{\text{syn}} &= \frac{2\pi k T_e \nu_c^3}{3hc^2} + 6.76 \times 10^{-28} \frac{n_i}{K_2(1/\theta_e) a_1^{1/6}} \\ &\times \left[\frac{1}{a_4^{11/2}} \Gamma\left(\frac{11}{2}, a_4 \nu_c^{1/3}\right) + \frac{a_2}{a_4^{19/4}} \Gamma\left(\frac{19}{4}, a_4 \nu_c^{1/3}\right) \right. \\ &\left. + \frac{a_3}{a_4^4} (a_4^3 \nu_c + 3a_4^2 \nu_c^{2/3} + 6a_4 \nu_c^{1/3} + 6) e^{-a_4 \nu_c^{1/3}} \right] \\ &\text{erg cm}^{-3} \text{ s}^{-1}, \end{aligned} \quad (15)$$

where

$$\begin{aligned} a_1 &= \frac{2}{3\nu_0 \theta_e^2}, \quad a_2 = \frac{0.4}{a_1^{1/4}}, \quad a_3 = \frac{0.5316}{a_1^{1/2}}, \quad a_4 = 1.8899 a_1^{1/3}, \\ \Gamma(a, x) &= \int_x^\infty t^{a-1} e^{-t} dt, \quad \nu_0 = \frac{eB}{2\pi m_e c} \text{ and } \nu_c = \frac{3}{2} \nu_0 \theta_e^2 x_M. \end{aligned} \quad (16)$$

Here B is the strength of the magnetic field and x_M is determined from the next equation as

$$\begin{aligned} \exp(1.8899 x_M^{1/3}) &= 2.49 \times 10^{-10} \frac{4\pi n_e r}{B} \frac{1}{\theta_e^3 K_2(1/\theta_e)} \\ &\times \left(\frac{1}{x_M^{7/6}} + \frac{0.40}{x_M^{17/12}} + \frac{0.5316}{x_M^{5/3}} \right). \end{aligned} \quad (17)$$

We give the magnetic field B at each radius, assuming that the ratio β of the magnetic energy density to the thermal energy density is constant throughout the region. The cooling rates due to the pair annihilation processes are neglected here because the equilibrium pair number density are found to be much smaller than the ion density in the present temperature region.

Finally, we set the outer boundary radius R_{out} to be $10^3 R_g$ and determine T_e , T_i and η using the adiabatic solutions so that the heating rate of electrons by ions equals to the bremsstrahlung cooling rate at $r = R_{\text{out}}$ and the total gas pressure $p = R_g \rho (T_e + T_i)$ has the same value as the adiabatic case. The flow variables of models A and B at the outer boundary are listed in Table 1.

2.2 Numerical results

We solve equations (3) – (5) inwards starting from the outer boundary using a second-order Runge-Kutta method. In

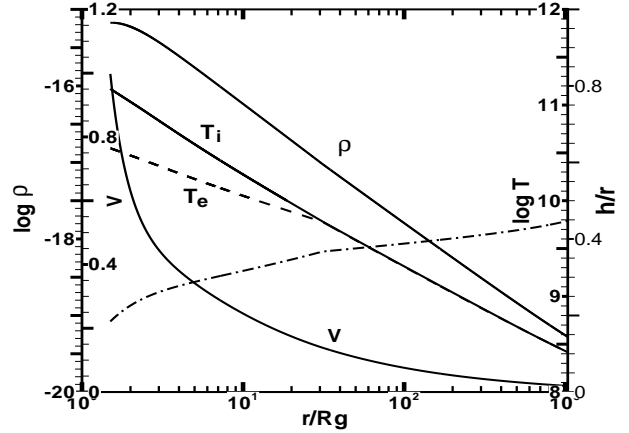


Figure 1. The radial velocity v , the ion temperature T_i , the electron temperature T_e (dashed line), the density ρ and the relative half thickness h/r of the accretion flow (dash-dotted line) for two-temperature model of model B with $\beta = 10^{-3}$. The distributions of these variable except T_e are almost same as those in one temperature model with $T_i = T_e$

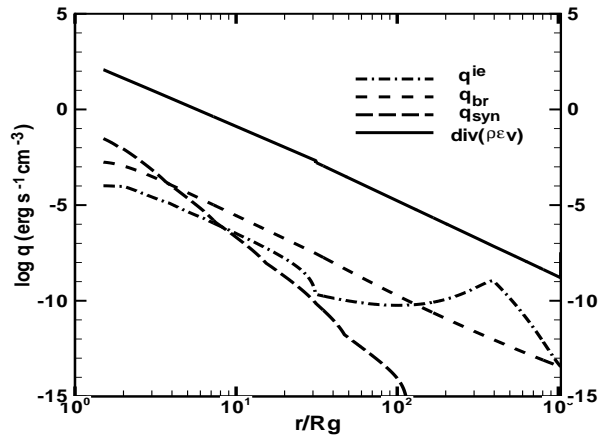


Figure 2. The energy transfer rate q^{ie} (dash-dotted line) from ions to electrons by Coulomb collisions, the bremsstrahlung cooling rate q_{br} (dashed line), the synchrotron cooling rate q_{syn} (long-dashed line) and the transfer rate $\text{div}(\rho \epsilon v)$ of the advected thermal energy versus radius in model B with $\beta = 10^{-3}$.

model A with $\beta = 10^{-3}$ and 1.0, we could not obtain the continuous flow solution which attains the inner boundary $R_{\text{in}} = 1.5R_g$ and the solution ended at $r \sim 4.2R_g$. If the effects of the radiative energy loss and gain are negligible, this is expected from the result of model A in the previous paper (Okuda & Molteni 2012), because the Mach number versus radius curve in the case would make a closed loop and never attain the event horizon. While, differently from model A, model B with $\beta = 10^{-3} - 1.0$ has the continuous solution to the inner edge. Fig. 1 shows the physical variables of the Mach number M_a of the radial velocity v , the ion temperature T_i , the electron temperature T_e , the density ρ and the half thickness of the accretion flow versus radius for model B with $\beta = 10^{-3}$. The electron temperatures deviate from the ion temperatures at $r/r_g \leq 30$ and the ratio T_i/T_e is ~ 4 at the inner edge. Table 2 shows the total integrated emission $\int q^{\text{ie}} dV$, $\int q_{\text{br}} dV$ and $\int q_{\text{syn}} dV$ for model B with $\beta = 10^{-3} - 1.0$. The synchrotron cooling rate depends on the magnetic field, that is, B and increases with increasing β , as is found from equations (15) and (16). As the result, we obtain total luminosities of $8.7 \times 10^{34} - 3.7 \times 10^{36}$ erg s^{-1} for model B with $\beta = 10^{-3} - 1.0$.

It should be noticed that the different temperatures of ions and electrons are caused only by the different adiabatic indices of ions and electrons and not by the effects of the radiative energy loss and gain. The transfer rate of the advected thermal energy fallen into the event horizon is much larger than the total amounts of the radiative heating and cooling. Fig. 2 shows the energy transfer rate q^{ie} (dash-dotted line) from ions to electrons, the bremsstrahlung cooling rate q_{br} (dashed line), the synchrotron cooling rate q_{syn} (longdashed line) and the transfer rate $\text{div}(\rho \varepsilon \mathbf{v})$ of the advected thermal energy versus radius in model B. The advected thermal energy term $\text{div}(\rho \varepsilon \mathbf{v})$ is by more than three orders of magnitude larger in the inner region compared with the cooling terms and balances exactly the rate $-p \text{div} \mathbf{v}$ of the internal energy increment by compression. Only the synchrotron cooling rate increases with increasing β and becomes comparable to the advected thermal energy term for the case of large $\beta (> 1)$. The adiabatic flow is due to the large radial velocity comparable to the free-fall velocity, the too low density of the gas and the large accretion flow thickness with $h/r \sim 1$. Accordingly, as long as the magnetic field is taken to be as $\beta \leq 1$, the effects of the radiative heating and cooling are negligible and the two-temperature model is ascribed to the adiabatic two-temperature model.

Thus, solving the 1D stationary differential equations, we get the accretion flow of model B but not of model A. However, we do not know yet whether the shock phenomena found in the previous paper occur or not and what accretion flow occurs actually in model A. The 1D flow equations also do not take account of the outflow which plays an important role in the actual accretion flow. Then, we examine the time-dependent 2D accretion flow.

3 TIME-DEPENDENT BEHAVIOURS OF 2D TWO-TEMPERATURE MODEL

3.1 Basic equations and methods

The set of relevant time-dependent equations are given in the spherical polar coordinates (r, ζ, φ) :

$$\frac{\partial \rho}{\partial t} + \text{div}(\rho \mathbf{v}) = 0, \quad (18)$$

$$\frac{\partial(\rho v)}{\partial t} + \text{div}(\rho v \mathbf{v}) = \rho \left[\frac{w^2}{r} + \frac{v_\varphi^2}{r} - \frac{GM}{(r - R_g)^2} \right] - \frac{\partial p}{\partial r}, \quad (19)$$

$$\frac{\partial(\rho r w)}{\partial t} + \text{div}(\rho r w \mathbf{v}) = -\rho v_\varphi^2 \tan \zeta - \frac{\partial p}{\partial \zeta}, \quad (20)$$

$$\frac{\partial(\rho r \cos \zeta v_\varphi)}{\partial t} + \text{div}(\rho r \cos \zeta v_\varphi \mathbf{v}) = 0, \quad (21)$$

$$\frac{\partial \rho \varepsilon_i}{\partial t} + \text{div}(\rho \varepsilon_i \mathbf{v}) = -p_i \text{div} \mathbf{v} - q^{\text{ie}}, \quad (22)$$

and

$$\frac{\partial \rho \varepsilon_e}{\partial t} + \text{div}(\rho \varepsilon_e \mathbf{v}) = -p_e \text{div} \mathbf{v} + q^{\text{ie}} - q_{\text{syn}} - q_{\text{br}}, \quad (23)$$

where $\mathbf{v} = (v, w, v_\varphi)$ are the three velocity components, ε_i and ε_e are the specific internal energy of the ion and electron. Here we neglect the radiation transport assuming that the flow is optically thin.

The set of partial differential equations (18)–(23) is numerically solved by a finite-difference method under adequate initial and boundary conditions. The initial flow variables are given from the 1D solutions in Section 2 but, at $r \leq 4.2R_g$ in model A, are given by extrapolation of nearby variables because the 1D solution of model A was obtained only at $4.2 \leq r/R_g \leq 10^3$. This approximation of the variables never influence the final result as long as the flow variables at the outer boundary are fixed constantly and a sufficiently large integration time is taken. The initial atmosphere above the accreting matter in the computational region is given as a radially hydrostatic equilibrium state with zero azimuthal velocities everywhere. Physical variables at the inner boundary, except for the velocities, are given by extrapolation of the variables near the boundary. However, we impose limit conditions that the radial velocities at the boundary are given by a free-fall velocity and the angular velocities are zero. As for the outer boundary region above the outer accreting matter, we use free-floating conditions and allow for the outflow of matter, whereas here any inflow is prohibited. With these initial and boundary conditions, we perform time integration of equations (18)–(23) until a quasi-steady solution is obtained.

3.2 Time variations of the luminosity and the mass-outflow rate

We show here the results of model A and B with $\beta = 10^{-3}$. The total luminosity L_T is a good measure to check whether a steady state of the accretion flow is attained and is given by $L_T = \int (q_{\text{br}} + q_{\text{syn}}) dV$. The mass-outflow rate \dot{M}_{out} is here given as the total flow rate of the outflow at the outer boundary. In model A, a shock is at first formed at $r \sim 15R_g$ on the equatorial plane, expands outwards gradually and finally moves up and down irregularly around $r \sim 50R_g$. Due to the modulation of the shock position, the total luminosity varies by a factor of 2 and the averaged one is 4.0×10^{36} erg s^{-1} . The mass-outflow rate also varies by a factor of ~ 4 and its averaged mass-outflow rate is as high as $\sim 1.0 \times 10^{20}$ g s^{-1} . About half of the input accreting matter is ejected as the wind. In model B, the shock wave appears in the inner region of $r \sim 19R_g$ which is a predicted value from the

Table 2. The integrated energies of q^{ie} , q_{br} and q_{syn} , respectively, by the Coulomb collision, the bremsstrahlung and the synchrotron for model B with $\beta = 10^{-3} - 1.0$.

β	Coulomb collision (erg s $^{-1}$)	Bremsstrahlung (erg s $^{-1}$)	Synchrotron (erg s $^{-1}$)
1.0	2.1×10^{35}	8.6×10^{34}	3.6×10^{36}
0.1	2.1×10^{35}	8.6×10^{34}	2.2×10^{35}
10^{-2}	2.1×10^{35}	8.6×10^{34}	1.3×10^{34}
10^{-3}	2.1×10^{35}	8.6×10^{34}	7.4×10^{32}

analysis in the 1D adiabatic case. Then, the shock moves outwards gradually, recedes inwards after attaining to a position of $\sim 140R_g$ and finally continues to oscillate irregularly between the radii of 45 and $65 R_g$. During the shock evolution, another weak shock appears inside the outer shock, disappears interacting with the outer shock and the inner edge and the processes are repeated irregularly. The shock phenomena cause the complicated modulations of the luminosity and the mass-outflow rate. Fig. 3 shows the time variations of the total luminosity L_T , the luminosity of the synchrotron radiation L_{syn} , the mass-outflow rate \dot{M}_{out} , the mass-inflow rate \dot{M}_{in} at the inner edge and the shock position R_s on the equatorial plane in model B. The total luminosity varies by a factor of 2 with time-scales of hours to days and the averaged luminosity is 2.5×10^{35} erg s $^{-1}$. The luminosity of the synchrotron radiation is 1.5×10^{33} erg s $^{-1}$ and varies largely by a factor of ~ 10 . The mass-outflow rate varies intermittently by a factor of 1.5, and the averaged value at later phases is 1.0×10^{19} g s $^{-1}$ which is several percent of the input matter. Accordingly, in this model, most of the input accreting matter falls into the event horizon through the inner edge.

The origin of the oscillating shock appearing in the present models is entirely attributed to the range of parameters of the specific energy and the specific angular momentum used here. The oscillatory shock is necessarily triggered if the specific angular momentum λ and the specific energy ϵ belong to or are located just nearby in the range of parameters responsible for a stationary shock in the rotating inviscid and adiabatic accretion flow, as is found in the previous paper.

Sgr A* possesses a quiescent state and a flare state. The flares and their quasi-periodicity of Sgr A* have been detected in multiple wavebands from radio, sub-millimetre, IR to X-ray (Genzel et al. 2003; Ghez et al. 2004; Eckart et al. 2006; Meyer et al. 2006a,b; Trippe et al. 2007; Yusef-Zadeh et al. 2009, 2011). The amplitudes of the flare at radio, IR and X-ray are by factors of below 1/2, 1–5 and 45 or even higher, respectively, a few times per day. The rapid variability in the radio band on time-scales of a few seconds to hours has been observed (Yusef-Zadeh et al. 2011). These flare phenomena are interesting in relation to the time variations of the luminosity. Actually, the modulation amplitude ~ 2 of the luminosity in models A and B can explain well the observed amplitudes of the variability at radio to IR except for the amplitude as high as ~ 45 at X-ray.

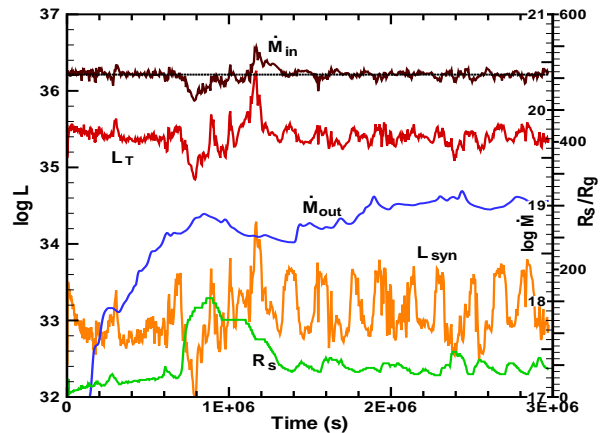


Figure 3. Time evolutions of total luminosity L_T (erg s $^{-1}$), the luminosity of the synchrotron radiation L_{syn} (erg s $^{-1}$), mass-outflow rate \dot{M}_{out} (g s $^{-1}$), mass-inflow rate \dot{M}_{in} (g s $^{-1}$) at the inner edge and shock position R_s (dotted line) on the equatorial plane in model B with $\beta = 10^{-3}$, where the dotted line shows the input accretion rate 2.44×10^{20} (g s $^{-1}$).

3.3 Structure of the flow and the shock

Fig. 4 shows the profiles of density ρ (g cm $^{-3}$), ion temperature T_i (K), electron temperature T_e , radial velocity v , Mach number M_a on the equatorial plane versus radius at $t = 2.8 \times 10^6$ s for model B with $\beta = 10^{-3}$. The outer shock and the weak inner shock are found at $r = 48$ and $10R_g$, respectively. The upstream electron temperatures in front of the outer shock equal to the ion temperatures but the downstream electron temperatures become to be lower than the ion temperatures in the post-shock region. The upstream electron adiabatic index γ_e ($=1.6$) changes into $4/3$ behind the shock. It is because the relation of the post-shock electron temperature $> T_e$ > the pre-shock electron temperature happens to be established here that the electron temperatures begin to deviate from the ion temperatures at the shock front. Both the electron and ion temperatures in the post-shock region are higher than those of the 1D stationary solution in Fig. 1 and the total luminosity 2.5×10^{35} erg s $^{-1}$ at this phase is high by a factor of 3 compared with 8.6×10^{34} erg s $^{-1}$ in the 1D solution.

Fig. 5 shows the contours of density ρ (g cm $^{-3}$) with velocity vectors at the same phase as Fig. 4 of model B. The outer shock extends obliquely upwards at $r \sim 48R_g$ on the equatorial plane. The initial accreting matter at the outer boundary supersonically falls down towards the gravitating centre and is decelerated at the shock front, enhancing the

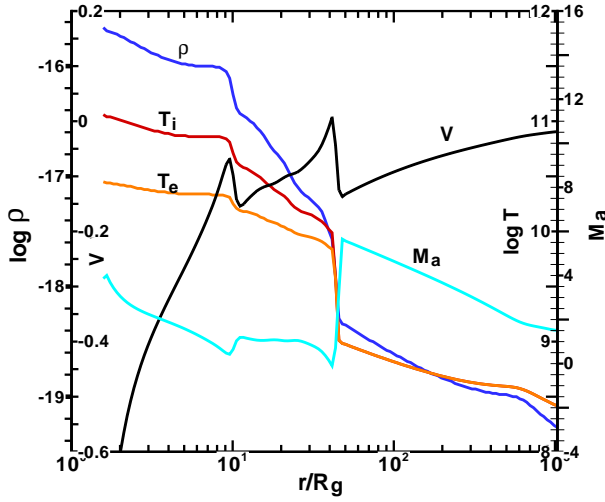


Figure 4. Profiles of density ρ (g cm^{-3}), ion temperature T_i (K), electron temperature T_e (K), radial velocity v and Mach number M_a of the radial velocity on the equatorial plane versus radius at $t = 2.8 \times 10^6$ s for model B with $\beta = 10^{-3}$. The outer shock and the inner weak shock are found at $r = 48$ and $10 R_g$, respectively.

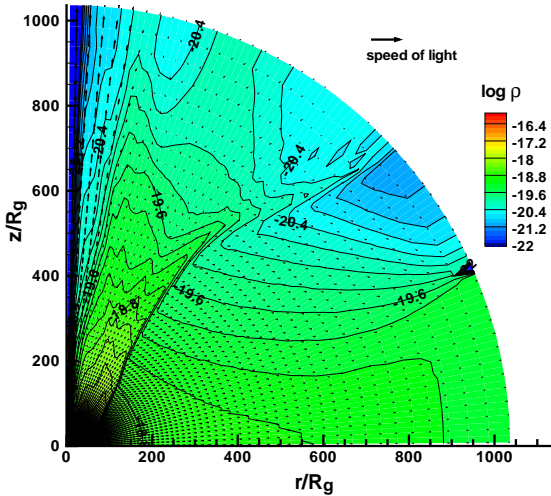


Figure 5. Contours of density ρ (g cm^{-3}) with velocity vectors at $t = 2.8 \times 10^6$ s of model B. The shock wave extends upwards obliquely at $r/R_g \sim 48$ on the equatorial plane.

density and the temperature, and becomes subsonic. The post-shock region with high densities and high temperatures results in a strong outward pressure-gradient force along the z -axis and a part of the accreting matter deviates from the disc flow and escapes as the wind flow. The mass-outflow begins only after the matter undergoes the shock compression. The wind velocities become $0.01\text{--}0.05c$ at the outer boundary except for a narrow funnel region along the z -axis where the flow is relativistic as $\sim 0.2\text{--}0.4c$.

Fig. 6 shows the energy spectra calculated from model

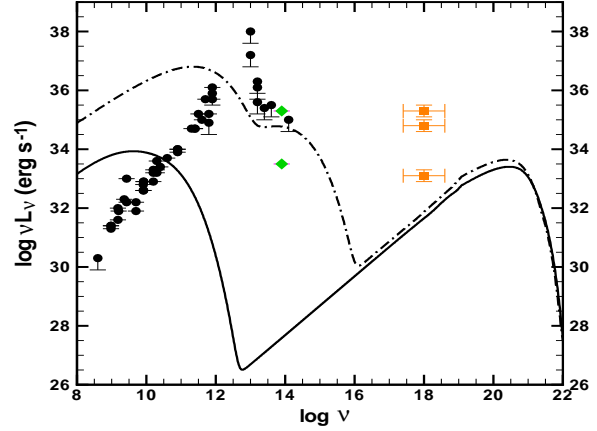


Figure 6. Energy spectra νL_ν (erg s^{-1}) of model B with $\beta = 10^{-3}$ (solid line) at $t = 2.8 \times 10^6$ s and initial model B with $\beta = 1.0$ (dash-dotted line), where the symbols of filled circle, diamond and cross are the observed data (Narayan et al. 1998; Baganoff et al. 2003; Genzel et al. 2003; Porquet et al. 2003; Ghez et al. 2004).

B with $\beta = 10^{-3}$ (solid line) at $t = 2.2 \times 10^6$ s, where the symbols of filled circle, diamond and cross show the observed points (Narayan et al. 1998; Baganoff et al. 2003; Genzel et al. 2003; Porquet et al. 2003; Ghez et al. 2004). The submillimetre and X-ray bumps in these spectra are originated from the synchrotron cooling by thermal electron and the bremsstrahlung cooling, respectively, whose formulas are prescribed in Stepney & Guilbert (1983) and Narayan & Yi (1995). The peak intensities in the submillimetre bumps in this model are low and the peak frequencies lie in longer wavelength compared with the observed spectra at the quiescent state of Sgr A*. To the contrary, the intensities in the X-ray band (~ 1 keV) are lower than the observed one but the X-ray spectra seem to be rather hard. In Table 2, we showed that the synchrotron emission increases with increasing β and the total luminosity is $\sim 10^{36}$ erg s^{-1} in model B with $\beta \sim 1$. For the comparison with the above spectra, we show the energy spectra of model B with $\beta = 1.0$ (dash-dotted line) in Fig. 6. The spectra for $\beta = 1.0$ in the radio to IR bands seem to be improved somewhat but are not sufficient to explain the observed one. The present simple model cannot reproduce the detailed spectra of Sgr A* as are successfully found in the ADAF models (Yuan, Quataert & Narayan 2003, 2004) but it is useful to examine the basic scenario of the low angular momentum flow model.

4 SUMMARY AND DISCUSSION

Following the previous paper based on the analysis of the angular momentum of the accretion flow around Sgr A* by Mościbrodzka, Das & Czerny (2006), we examined a low angular momentum flow model for Sgr A* using 1D stationary and 2D time-dependent hydrodynamical calculations under the two-temperature model. Adopting the model param-

ters of the specific angular momenta λ of 1.35 and 1.68 and the input accretion rates of $\dot{M}_{\text{input}} = 4.0 \times 10^{-6} M_{\odot} \text{ yr}^{-1}$, we summarize the results as follows.

(1) As long as the ratio β of the magnetic energy density to the thermal energy density is taken to be as $\beta \leq 1$, the radiative energy loss and gain due to the Coulomb collisions, the bremsstrahlung and the synchrotron emissions are negligible on the dynamics of the flow and the two-temperature model is ascribed to the adiabatic two-temperature model.

(2) The different temperatures of ions and electrons are caused by the different adiabatic indices of ions and electrons which depend on their temperature states under the relativistic regime. The total luminosity increases with increasing β and results in $\sim 10^{35} - 10^{36} \text{ erg s}^{-1}$ for $\beta = 10^{-3} - 1.0$ which is comparable to the observed luminosity of Sgr A*.

(3) Due to the constant low angular momentum flow, the irregularly oscillating shocks are formed in the inner region, as is found in the previous paper, and the luminosity and the mass-outflow rate are modulated by a factor of 2 – 3 and 1.5 – 4, respectively, on time-scales of hours to days.

(4) The time variability may be related to the flare phenomena of Sgr A*.

Further evidence of the low angular momentum of the accretion flow around Sgr A* would confirm the validity of the model. If the specific angular momentum of the accretion flow around Sgr A* is actually as small as $\lambda=1.35 - 1.68$, the time variabilities of the total luminosity found in models A and B may explain the quiescent and flare states of Sgr A* at the radio to IR bands except for X-rays. However, there remain important problems of the too high X-ray variability and the time lag between the radio and X-ray flares in Sgr A*. In stead of this scenario for the flare activity of Sgr A*, we may interpret alternative one for the quiescent and flare states of Sgr A*, somewhat on the analogy of the temporal sequence of accretion disc-jet coupling observed in the X-rays, IR and radio wavelengths of the microquasar GRS 1915+105 (Mirabel et al. 1998). Then we regard the total emission obtained in the models as the permanent emission of the quiescent state but consider that the emission variabilities in Sgr A* are caused by the intermittent outflow found in the present models, where the mass-outflow rates are as high as $2 \times 10^{-7} - 2 \times 10^{-6} M_{\odot} \text{ yr}^{-1}$ and vary by a factor of 1.5 – 4 and the outflow escapes as the high-velocity jets with $0.01 - 0.2c$ along the rotational axis. We speculate here that the intermittent high-velocity jets propagate outwards, interact with the surrounding matter and excite the matter as a hot emitter. The emission from the hot matter may be observed as an amplified flare in X-rays. After that, the high-velocity jets expand furthermore, cool down adiabatically, interact again with the distant interstellar cloud and emit radio emission which is observed as a radio flare with a time lag. In the present models, we have treated only the inviscid accretion flow. If the accretion flow is actually viscous flow in Sgr A* system, the present result of the low angular momentum flow model will be changed largely and the application of the shock phenomena to the time variability of Sgr A* will be invalid because of no shock formation. The present low angular momentum flow model is also simple and cannot reproduce the detailed observed spectra of Sgr A*. For the spectral fitting with the observations, we need to treat the physics of the synchrotron and

inverse Compton emission by the thermal and non-thermal electrons. A further magneto-hydrodynamical examination of the flow with the low angular momentum including the above physics should be pursued in the future.

ACKNOWLEDGEMENTS

I thank an anonymous referee for useful suggestion of the adiabatic index effects of ions and electrons on the two-temperature model.

REFERENCES

- Baganoff F. K., et al. 2003, ApJ, 591, 891
- Bondi H., 1952, MNRAS, 112, 195
- Chakrabarti S. K., 1989, ApJ, 347, 365
- Czerny B., Mościbrodzka M., 2008, J. Phys. Conf. Ser., 132, 012001
- Eckart A., Schödel R., Meyer L., Trippe S., Ott T., Genzel R., 2006, A&A, 455, 1
- Esin A. A., Narayan R., Ostriker E., Yi I., 1996, ApJ, 465, 312
- Fukue, J., 1986, PASJ, 38, 167
- Genzel R., Schödel R., Ott T., Eckart A., Alexander T., Lacombe F., Rouan D., Aschenbach B., 2003, Nature, 425, 934
- Ghez A. M., et al. 2004, ApJ, 601, L159
- Meyer L., Schödel R., Eckart A., Karas V., Dovčiak M., Duschl W.J., 2006a, A&A, 458, L25
- Meyer L., Eckart A., Schödel R., Duschl W.J., Mužić K., Dovčiak M., Karas, V., 2006b, A&A, 460, 15
- Mirabel L. F., Dhawan V., Chaty S., Rodríguez L. F., Martí J., Robinson C. R., Swank J., Geballe T. R., 1998, A&A, 330, L9
- Mościbrodzka M., Das T.K., Czerny B., 2006, MNRAS, 370, 219
- Nakamura K. E., Matsumoto R., Kusunose M., Kato S., 1996, PASJ, 48, 761
- Narayan R., Mahadevan R., Grindlay J. E., Popham R. G., Gammie C., 1998, ApJ, 492, 554
- Narayan R., McClintock J.E., 2008, New Astron. Rev, 51, 733
- Narayan R., Yi I., 1994, ApJ, 428, L13
- Narayan R., Yi I., 1995, ApJ, 452, 710
- Okuda T., Molteni D., 2012, MNRAS, 425, 2413
- Porquet D., Predehl P., Aschenbach B., Gross N., Goldwurm A., Goldoni P., 2003, A&A, 407, L17
- Shakura N.I., Sunyaev R.A., 1973, A&A, 24, 337
- Stepney S., Guilbert P.W., 1983, MNRAS, 204, 1269
- Trippe S., Paumard T., Ott T., Gillessen S., Eisenhauer F., Martins F., Genzel, R., 2007, MNRAS, 375, 764
- Yuan F., 2011, in Morris M.R., Wang Q.D., Yuan F., eds, ASP Conf. Ser. 439, The Galactic Center: A Window to the Nuclear Environment of Disk Galaxies. Astron. Soc. Pac., San Francisco, p. 346
- Yuan F., Narayan R., 2014, ARA&A, vol.52, preprint (arXiv:1401.0586)
- Yuan F., Quataert E., Narayan R., 2003, ApJ, 598, 301
- Yuan F., Quataert E., Narayan R., 2004, ApJ, 606, 894
- Yusef-Zadeh F. et al., 2009, ApJ, 706, 348

Yusef-Zadeh F., Wardle M., Miller-Jones J.C.A., Roberts
D.A., Grosso N., Porquet D., 2011, ApJ, 729, 44